Journal of Materials Chemistry A

Accepted Manuscript

ROYAL SOCIETY OF CHEMISTRY

www.rsc.org/materialsA

Role of Cr^{3+}/Cr^{6+} Redox in Chromium-substituted Li_2MnO_3•$LiNi_{1/2}Mn_{1/2}O_2$ Layered Composite Cathodes: Electrochemistry and Voltage Fade

Eungje Lee[1,*], Joong Sun Park[1], Tianpin Wu[2], Cheng-jun Sun[2], Hacksung Kim[1,3], Peter C. Stair[1,3], Jun Lu[1], Dehua Zhou[1,4], and Christopher S. Johnson[1]

[1]Chemical Sciences and Engineering Division, Argonne National Laboratory, Argonne, IL 60439, USA

[2]Advanced Photon Source, Argonne National Laboratory, Argonne, IL 60439, USA

[3]Catalysis Center, Northwestern University, Evanston, IL 60208, USA

[4]Department of Chemical Engineering, University of Rochester, Rochester, NY, 14627, USA

[*]Corresponding Author:
E-mails: eungje.lee@anl.gov (E. Lee)

Abstract

The effect of redox-active Cr substitution on the electrochemistry and voltage fade of a lithium-rich "layered-layered" composite cathode material has been investigated. A series of Cr-substituted $0.5Li_2MnO_3 \bullet 0.5LiNi_{1/2}Mn_{1/2}O_2$ powder samples (i.e., $Li_{1.2}Ni_{0.2-2/x}Mn_{0.6-2/x}Cr_xO_2$, where x = 0, 0.05, 0.1, and 0.2) was synthesized via the sol-gel method. X-ray diffraction data confirmed the incorporation of Cr ions into the lattice structure. While similar initial charge capacities (~300 mAh/g) were obtained for all of the cathode samples, the capacity contribution from the Li_2MnO_3 activation plateau (at 4.5 V vs. Li) decreased with increasing Cr content. This finding suggests suppressed oxygen loss that triggers cation migration and voltage fade in subsequent cycles. Continued investigation revealed that the Cr substitution mitigates the voltage fade on charge but not discharge. The resulting insignificant effect of Cr substitution on mitigating voltage fade, in spite of decreased Li_2MnO_3 activation, is attributed to the additional instability caused by Cr^{6+} migration to a tetrahedral site, as evidenced by *ex-situ* X-ray absorption spectroscopy. Our results provide the framework for future redox active cation substitution strategy by highlighting the importance of the structural stability of the substituent itself.

Key words: batteries; lithium-ion; layered oxide; voltage fade

1. Introduction

The success of lithium-ion batteries for energy storage in portable electronic devices during the past decades is now driving their application to a more challenging level; vehicle electrification. The energy density of commercial lithium-ion cells has been continuously improved, mainly by the advancement of battery manufacturing techniques; however, the requirements for vehicular applications are very demanding such that it is imperative to develop advanced materials that can overcome the intrinsic limitations in current electrodes and electrolytes.[1-3] Among various cathode candidates, lithium- and manganese-rich transition metal layered oxides (LMR-NMC) are attracting much interest.[4] In LMR-NMC materials, the excess lithium ions occupying transition metal sites are preferentially surrounded by manganese ions, resulting in nano-scale Li_2MnO_3 and $LiMO_2$ (M = transition metals such as Ni, Mn, and Co) ordered domains that are crystallographically integrated.[5-7] Such a nano-composite "layered-layered" structure provides unique electrochemical properties that are different from those of the single-phase end members, Li_2MnO_3 and $LiMO_2$.[5] Typical specific capacities are well over ~250 mAh/g, with an average voltage of ~3.8 V vs. Li; the resulting energy density is more than ~900 Wh/kg, which could meet the energy density requirements of cathodes for plug-in hybrid electric vehicles (PHEVs) and full electric vehicles (EVs).[8] In addition, the higher content of manganese makes the LMR-NMC materials even more attractive, since manganese is less expensive, thermally more stable, and environmentally benign compared with cobalt and nickel.

The high energy density and excellent capacity retention of the LMR-NMC materials have been well known for a long time; however, only recently was it reported

that the average equilibrium voltage of LMR-NMC continuously decreases during high-voltage cycling.[9] This voltage fade causes not only a continuous reduction in energy density of the cell but also difficulties in battery management. With respect to the latter, the determination of state of charge and subsequent cell management becomes complicated if the average voltage continuously changes with progressive cycles. Understanding and arresting the voltage fade, therefore, are urgently required for commercialization of LMR-NMC cathodes.

The voltage fade is related to irreversible phase relaxation via migration of cations. During the first charge, the voltage profile shows a sloping curve corresponding to Ni and/or Co oxidation until 4.5 V, and then it turns into a flat plateau at above 4.5 V, where the activation of the Li_2MnO_3 component occurs.[5] Although the detailed mechanisms underlying the activation process remain to be determined, it has been generally accepted that the removal of excess lithium ions during the activation accompanies concomitant oxygen loss.[10, 11] The formation of lithium and oxygen vacancies increases the structural instability and triggers irreversible cation migration facilitated by the formation of oxygen vacancies, which leads to local structural transformation from the layered to spinel-like cation arrangement.[12-15] This structural relaxation results in a cycle-to-cycle voltage fade in the LMR-NMC materials.

A common practice in evaluating the degree of voltage fade is to compare the shape changes in the discharge voltage profiles after an extended number of cycles. However, such qualitative evaluations require meticulous attention in data interpretation because the significant contribution from electrode impedance (a kinetic parameter) can screen out the contribution from the equilibrium voltage change (a thermodynamic

parameter). To address this problem, researchers at Argonne National Laboratory have devised a voltage-fade test protocol to measure the change in resistance-corrected quasi-equilibrium average voltages at each cycle.[9] Using the test protocol, they showed that surface modifications via coatings and electrolyte additives reduce electrode impedance, but do not suppress the voltage fade.[16, 17] These results reconfirmed that the voltage fade in LMR-NMC is not a surface issue but a bulk structural issue. Lee et al.[18, 19] also attempted structural stabilization through the substitution of redox-inactive cations (Al, Ga, and Fe, max. 10%); however, the voltage fade tests revealed no meaningful effects. The ineffectiveness of the small degree of substitution is understandable when the severe structural changes that LMR-NMC would experience during the activation process is considered. Considering the role of oxygen loss, the layered-layered structure may have a strong driving force that rearranges the cation positions and transforms the material to a lower energy phase. This driving force may not be stopped by only a small degree of cation substitution. A large degree of redox-inactive cation substitution, instead, would decrease the reversible capacity significantly, making this solution ineffective.

Herein, we report the effect of Cr substitution on the voltage fade in layered-layered cathode materials. Compared to the redox-inactive cation substitutions, the redox active Cr can be substituted to higher degrees without a significant sacrifice in reversible capacity. Furthermore, the three-electron transfer process of Cr^{3+}/Cr^{6+} redox could provide the charge compensation required for high capacity cycling and eliminate the necessity for the Li_2MnO_3 activation, which triggers structural instability and voltage fade. Although the electrochemical performance of the Cr-containing layered-layered composite materials has been reported by several groups,[20-23] their voltage fade behavior

has never been systematically evaluated, to the best of our knowledge. Therefore, we synthesized a series of $Li_{1.2}Ni_{0.2-x/2}Mn_{0.6-x/2}Cr_xO_2$ samples ($0.5Li_2MnO_3 \bullet 0.5LiNi_{0.5-y/2}Mn_{0.5-y/2}Cr_yO_2$ in composite notation) by the sol-gel method and tested the effect of Cr substitution on the electrochemical performance, particularly with respect to the voltage fade.

2. Experimental Methods

Electrode materials with a nominal composition of $Li_{1.2}Ni_{0.2-x/2}Mn_{0.6-x/2}Cr_xO_2$ (x = 0, 0.05, 0.1, and 0.2) were prepared by sol-gel reaction of metal acetates and glycolic acid in water solvent. Stoichiometric amounts of $Li(CH_3COO) \bullet 2H_2O$ (≥99.0%, Sigma-Aldrich Co.), $Ni(CH_3COO)_2 \bullet 4H_2O$ (≥99.0%, Sigma-Aldrich Co.), $Mn(CH_3COO)_2 \bullet 4H_2O$(Sigma Aldrich Co.), and $Cr(NO_3)_3 \bullet 9H_2O$ (Sigma Aldrich Co.) were completely dissolved in deionized water. This solution was then mixed with an aqueous solution of glycolic acid, and the pH was adjusted to ~7 by adding ammonium hydroxide. The mixed solution was heated at ~75^{o}C and vigorously stirred until a transparent gel was obtained. After decomposition of the gel product in a furnace at 400^{o}C for 12 h in air, the obtained powder was thoroughly ground and heat treated at 850^{o}C for 12 h in air.

The elemental and morphological analyses of the as-synthesized powder materials were performed by, respectively, inductively coupled plasma-mass spectrometry (ICP-MS) and scanning electron microscopy (Hitachi S-4700 FE-SEM). X-ray diffraction (XRD) was conducted with CuKα radiation, whereby the lattice parameter was calculated by the whole powder pattern decomposition method assuming the space group of R-3m. UV Raman spectra were recorded with a triple-grating spectrometer (Princeton

Instruments, Trivista 555) equipped with a liquid N_2-cooled CCD detector using 325 nm radiation from a He-Cd laser (Kimmon) for excitation. The measurement was conducted in Ar atmosphere at room temperature. The laser power delivered to the sample was 2 mW. A home-made ellipsoidal reflector with the backscattering geometry was used to collect the scattered light. The Raman shift was calibrated with cyclohexane and chloroform. The accuracy of Raman shift is estimated to be ±1 cm^{-1}. X-ray absorption spectroscopy (XAS) measurements at the Cr-K edge (5989 eV) were carried out at beamline 20-BM-B of the Advanced Photon Source (APS) at Argonne National Laboratory. Measurements were made in the transmission mode. A chromium foil spectrum was acquired for energy calibration. Standard procedures based on Athena software were used to fit the XAS data.

Electrochemical performance was evaluated with 2032-type coin cells prepared in an Ar-filled glovebox (O_2 < 10 ppm, H_2O < 1 ppm). A cathode slurry was prepared with active materials, Super P-Li carbon (Cabot Co.), and polytetrafluoroethylene (PVDF, Solvay) in 84:8:8 ratio. This slurry was then coated on aluminum foil, and the dried laminate was calendared to ensure intimate contact between particles. A typical active material loading was 5 mg/cm^2. The anode was a lithium metal disc, and the electrolyte consisted of 1.2 M $LiPF_6$ in a mixture of ethylene carbonate and ethyl methyl carbonate (3:7 by volume). These coin cells were tested galvanostatically at ambient temperature according to a protocol developed to track the changes in quasi-equilibrium voltage. The details of the cycling protocol are explained elsewhere.[9] Briefly, the first cycle was conducted at a current rate of 10 mA/g in a voltage range of 2–4.7 V vs. Li for activation, and then the current rate was increased to 20 mA/g for the following cycles. From the

second cycle onwards, current interrupt measurements were carried out to estimate cell resistance at various voltages (3.5, 3.9, and 4.3 V during charge and at 4.0, 3.6, and 3.2 V during discharge). The current was stopped for 10 min, and the voltage differences were recorded to obtain the cell resistance (i.e., dV/dI). The average cell resistance (R_{avg}) was then subtracted from the average cell voltage ($V_{avg} = E/Q = (1/Q)\int V(q)dq$, where V_{avg}, E, and Q are average cell voltage, total energy, and capacity, respectively) to calculate the resistance-corrected average voltage ($V_{avg, iR\text{-}corr}$).

3. Results and Discussion

3.1. Morphology and structure of as-synthesized samples

The chemical composition of the as-synthesized $Li_{1.2}Ni_{0.2-x/2}Mn_{0.6-x/2}Cr_xO_2$ (x = 0, 0.05, 0.1, and 0.2) was confirmed by ICP-MS analysis. The measured compositions are very close to the target compositions listed in Table 1. Figure 1 compares the particle morphology of as-synthesized powder samples for the different values of x. The x = 0 sample shows aggregations of spherical primary particles having average particle size of ~0.3 μm. In contrast, the SEM images of the Cr-substituted samples show both small spherical particles (~0.3 μm) and larger faceted particles (~1.0 μm), suggesting abnormal grain growth resulting in a bimodal particle-size distribution.[24] The overall increase in the particle size as a result of Cr substitutions is consistent with previous reports.[21, 23]

In Fig. 2a, all of the as-synthesized samples show a typical XRD pattern for LMR-NMC materials. Because of the structural compatibility of layered $LiNi_{0.5}Mn_{0.5}O_2$ and Li_2MnO_3 compounds, all the strong peaks are indexed to a trigonal R-3m symmetry while several weak peaks at 20 - 28^o are indexed to the monoclinic C2/m unit cell. These

weak superstructure peaks, which are magnified in the inset of Fig. 2a, are the characteristic of the $LiMn_6$ cation ordering that occurs in the transition metal layers of Li_2MnO_3.[5-7] Compared to the x = 0 sample, the low degree of Cr substitution (x = 0.05 and 0.1) resulted in more pronounced superstructure peaks. This is consistent with previous observations by Singh et al.[25] The increasing intensity for the superstructure peaks in the x = 0.05 and 0.1 samples indicates stronger tendency for Li-Mn ordering that results in (1) larger in-plane $LiMn_6$ ordered domains and/or (2) higher c-axis correlation of the $LiMn_6$ ordered domains. However, the superstructure peaks become broader for the x = 0.2 sample. This may be due to the excessive amount of Cr ions that had perturbed the Li-Mn ordering.

Close inspection of the XRD pattern for the x = 0 sample revealed additional shoulder peaks at the lower 2θ side of the (104) and (101) peaks. These peaks can be attributed to the spinel component such as $LiMn_{1.5}Ni_{0.5}O_4$.[26] The cubic closed packing in layered and spinel lithium metal oxide is structurally compatible and the spinel component can be easily incorporated into the layered structure. In general, the spinel component is observed when the lithium content is reduced from the stoichiometric layered-layered composition, such as $Li_{1.2-y}Ni_{0.2}Mn_{0.6}O_2$ (y > 0).[27-29] Therefore, it is interesting to observe a spinel component in our x = 0 sample that has the stoichiometric lithium content (y = 0) as confirmed by the elemental analysis (Table 1). We presume that (1) the identical transition metal ratio (Ni:Mn = 1:3) in both the x = 0 sample and the $LiNi_{0.5}Mn_{1.5}O_4$ spinel phase and (2) the sol-gel synthesis condition used in this study provide more favorable conditions for precipitation of a spinel component during the synthesis of $Li_{1.2}Ni_{0.2}Mn_{0.6}O_2$. Indeed, we have observed in a separate sol-gel synthesis

study that the amounts of a spinel component in the same layered-layered composition are dependent on synthesis conditions. However, the trace amount of spinel in our x = 0 sample shows only a negligible electrochemical effect in the scope of this study, and we will treat it as like an impurity phase.

Table 2 summarizes the lattice parameters and unit cell volumes of the as-synthesized $Li_{1.2}Ni_{0.2-x/2}Mn_{0.6-x/2}Cr_xO_2$ samples. The unit cell volumes proportionally increase with increasing Cr content. Previous studies on $Li_{1.2}Mn_{0.4}Cr_{0.4}O_2$ ($0.5Li_2MnO_3$•$0.5LiCrO_3$ in composite notation) and $LiNi_{0.5-x/2}Mn_{0.5-x/2}Cr_xO_2$ showed that the as-synthesized samples have nickel, chromium, and manganese ions in the divalent, trivalent, and tetravalent state, respectively.[21, 30] Therefore, the systematic increase in unit cell volume as a result of Cr substitution corresponds well to the addition of larger Cr^{3+} ($\boldsymbol{r}_{Cr}{}^{3+}$ = 0.615 Å) at the expense of smaller Ni^{2+}/Mn^{4+} in the 1:3 ratio ($\boldsymbol{r}_{1/4Ni}{}^{2+}$•$_{3/4Mn}{}^{4+}$ = 0.57 Å). This proportional relationship between Cr content and unit cell volume in $Li_{1.2}Ni_{0.2-x/2}Mn_{0.6-x/2}Cr_xO_2$ supports the effective incorporation of Cr ions into the parent lattice structure. Considering the relatively lower charge ordering effect between the Li^+ and Cr^{3+} ions, it is presumed that the Cr^{3+} ions are substituted into the $LiMO_2$ layered domains instead of the Li_2MnO_3 domains where strong Li^+ and Mn^{4+} orderings presence. Nevertheless, it should be noted that more detailed analysis is required to determine the precise position of substituted Cr ions, and this topic remains in the works for a future study.

Figure 2b shows UV Raman spectra of the samples with x = 0, 0.05, 0.1, and 0.2. The spectrum of the sample with x = 0 shows Raman bands at 433 cm^{-1}, 488 cm^{-1}, and 605 cm^{-1}, which match well with the characteristic Raman bands of Li_2MnO_3.[25, 31] The

band at 433 cm^{-1} has been found to be due to Li-O vibrations.[32] The other two strong bands are assigned to Mn-O vibrations of the totally symmetric A_g mode (C_{2h} symmetry).[31] The sample with x = 0.2 also shows the characteristic Raman features of Li_2MnO_3, but at a little lower frequencies by 4 cm^{-1} for 605 cm^{-1} band and by 5 cm^{-1} for 488 cm^{-1} band. Raman positions of the samples with x = 0.05 and 0.1 appear in the middle of those of the two end samples, x = 0 and 0.2. The redshift in position can be explained by a slight elongation of Mn-O bonds by the interaction of Cr and oxygen in Mn-O bonds.

3.2. Electrochemical performance

Figure 3 compares the initial voltage profiles of $Li_{1.2}Ni_{0.2-x/2}Mn_{0.6-x/2}Cr_xO_2$. The charge curve for the x = 0 sample shows a typical voltage response of the "layered-layered" composite cathodes characterized by an initial voltage slope followed by a long voltage plateau at 4.5 V. The initial slope and subsequent 4.5 V plateau are attributed to the Ni^{2+}/Ni^{4+} redox reaction and activation of Li_2MnO_3 domain, respectively.[5] Compared to the x = 0 electrode, the initial charge curves of the Cr-substituted electrodes (x = 0.05, 0.1, and 0.2) show larger voltage slope and shorter 4.5 V plateau. Table 3 summarizes the initial capacity contributions from each region. While all of the samples have similar total capacities during the first charge, the capacity contribution from the slope region proportionally increases with Cr substitution from 98.3 mAh/g for the x = 0 electrode to 191.6 mAh/g for the x = 0.2 electrode. This difference is presumably associated with a charge compensation in the initial slope region for the Cr-substituted samples being accomplished by the simultaneous oxidation of the Ni^{2+}/Ni^{4+} and Cr^{3+}/Cr^{6+} redox couples.

The Cr^{3+}/Cr^{6+} redox reaction can deliver three electrons per cation, which is higher than the two-electron delivery of the Ni^{2+}/Ni^{4+} redox.[20, 21, 30] Therefore, more Li ions can be deintercalated from the Cr-substituted electrodes before the activation of Li_2MnO_3 domains.

Observing the higher charge compensation from the Cr^{3+}/Cr^{6+} redox reaction, one may expect higher total initial charge capacity for the Cr substituted samples assuming the same amount of Li_2MnO_3 activation for all samples. However, the initial charge capacity contribution from the Li_2MnO_3 activation actually decreases with Cr substitution and the similar total charge capacities are obtained from all of the samples regardless of Cr substitution. The irreversible activation of Li_2MnO_3 is because the Mn oxidation is replaced by the oxidation of the ligand due to the high covalency in the bonds between empty e_g orbitals of Mn^{4+} and oxygen *p* orbitals. Therefore, the decrease in the activation capacity with Cr substitution may suggest that the oxidation of Cr^{3+} to Cr^{6+} changes the covalency of Mn(IV)-O bonds and reduces the degree of Li_2MnO_3 activation. Considering the negative effect that Li_2MnO_3 domain activation has on the initial irreversible capacity and structural instability, it is encouraging that the capacity contribution from the 4.5 V plateau in the x = 0.2 electrode (105.8 mAh/g) is only half that in the baseline (x = 0) electrode (206.4 mAh/g), while both electrodes show similar total charge capacities.

The subsequent discharge capacity decreases with increasing Cr content, resulting in lower initial coulombic efficiency for the Cr-substituted samples. The higher first-cycle irreversibility in the Cr-substituted samples, in spite of the decreased degree of Li_2MnO_3 activation, suggests that the Cr^{3+}/Cr^{6+} redox may involve an irreversible

contribution during the first charge-discharge. To confirm this irreversible contribution, the coin cells were cycled between 2.0 and 4.2 V because, in this voltage range, the irreversible capacity from the Li_2MnO_3 activation is excluded. In Fig. 4, the initial charge capacity increases with increasing Cr substitution, corresponding to the increasing contribution of the Cr^{3+}/Cr^{6+} redox. However, the Cr substitution decreases the coulombic efficiency for the first cycle. For instance, the initial charge capacity for the x = 0.2 electrode (125 mAh/g) is greater than that for the x = 0.1 electrode (103 mAh/g), whereas the subsequent discharge capacity for the x = 0.2 electrode is only 88 mAh/g, compared to 95 mAh/g for the x = 0.1 electrode. This difference is due to the greater extent of irreversibility in the x = 0.2 electrode.

The negative effect of Cr substitution on the initial coulombic efficiency was investigated by *ex-situ* XAS. Figure 5 shows the normalized Cr K-edge X-ray absorption near edge structure (XANES) for the x = 0.2 electrode at different states of charge. The edge position in the XANES curve for the pristine electrode is very similar to the one for $LiCrO_2$[22] and is attributed to Cr^{3+}. During charging, the Cr K-edge position in Fig. 5 shifts rigidly to higher energies, and the pre-edge peak intensity increases significantly. The prominent pre-edge peak in the XANES for chromium is a well-known marker for tetrahedral Cr^{6+} ions.[30] These results indicate the oxidation and migration of Cr^{3+} in an octahedral site to Cr^{6+} in a tetrahedral site on charging. When discharged to 2.0 V, the Cr K-edge shifts back to lower energy, and the intensity of the pre-edge peak decreases due to the reduction of Cr^{6+} to Cr^{3+}. However, the Cr K-edge position is not as low as what is seen for the pristine electrode, and the significant intensity for the pre-edge peak is still observable. This finding corroborates that oxidation and migration of Cr^{3+} to Cr^{6+} are

only partially reversible, and considerable amounts of Cr^{6+} ions are stranded in the tetrahedral sites and do not return to octahedral sites even at the end of discharge during the first cycle.[30,33]

Figure 6 shows that the low initial coulombic efficiencies of the Cr-substituted samples improve in subsequent cycles and reach ~100% within 1 – 3 cycles. The recovery of high coulombic efficiencies after several cycles suggests that the irreversible migration of Cr^{6+} ions to tetrahedral sites occurs only at the first few cycles. Upon further cycling, the Cr^{3+}/Cr^{6+} redox reaction occurs reversibly, accompanied by reversible shuttling of Cr ions between the octahedral and tetrahedral sites.[30, 33] As shown in Fig. 6, all of the samples exhibit good cycle performance.

3.3. Voltage fade test

In general, electrode impedance gradually increases during continuous cycling as a result of various cell degradation mechanisms, such as surface film formation and loss of intimate contact between particles. The subsequently increasing cell overpotentials, then, open up the charge-discharge voltage windows by raising the charge curves to the direction of higher voltage and depressing the discharge curves to the direction of lower voltage. However, in LMR-NMC, the effect from voltage fading becomes dominant over the effect from the impedance rise, and both charge and discharge curves together shift towards lower voltage. Figure 7a clearly shows the voltage fade in the x = 0 electrode, with a faster depression in the low voltage segment (below 3.6 V) than the high voltage segment (above 3.6 V). As a result, the voltage curve at the 50th cycle has a clear inflection point that divides the voltage curve into two apparent segments around 3.6 V.

The normalized differential capacity (1/Q*(dQ/dV)) plots for the x = 0 electrode in Fig. 8a also exhibit the corresponding peak shifts: the charge peak at ~3.2 V (peak I) grows stronger and shifts to lower voltage at the expense of the peak at ~4.4 V (peak III). The charge peak at ~3.8 V (peak II) maintains its intensity and position. The irreversible shifts in the differential capacity plots on cycling are ascribed to the transformation of an initial phase that is redox active at high potential (peak III) into one or more redox-active phases located at low potential (peak I).[9, 34]

The Cr-substituted electrodes also exhibit the voltage fade in Figs. 7b-d. However, careful examination reveals that the cycled voltage curves maintain their initial curve shape better than the pristine electrode despite the overall decrease in average voltages. The development of an inflection point in the charge-discharge curves such as in Fig. 7a is not observed. The corresponding differential capacity plots in Figs. 8b-d also confirm the less pronounced changes in 1/Q*(dQ/dV) peaks compared to the plot in Fig. 8a. For example, the x = 0.1 and 0.2 electrodes show major peak reduction at ~3.8 V (peak II) instead of ~4.4 V (Peak III) during both charge and discharge. These different modes of voltage fade in the Cr-substituted electrodes could be attributed to the tetrahedral Cr^{6+} ions. The manganese-dominated transition metal migration may be deflected, although not prevented, by the irreversibly oxidized tetrahedral Cr^{6+} species and the quasi-reversible migration of Cr^{3+} and Cr^{6+} between the octahedral and tetrahedral sites.

The effect of Cr substitution on voltage fade was quantitatively evaluated after the impedance effect on the apparent voltage change was determined in the voltage-fade test protocol.[9, 17] The average resistance at each charge or discharge step was obtained for

interrupts in the area specific current and was subtracted from the average voltage (V_{avg}) to calculate the resistance-corrected average voltage ($V_{avg, iR\text{-}corr}$). The changes in V_{avg} and $V_{avg, iR\text{-}corr}$ for the x = 0 and 0.1 electrodes are plotted as a function of cycle number in Fig. 9. While the x = 0.1 electrode has higher overall voltage compared to the x = 0 electrode, both electrodes show continuous decrease in V_{avg} and $V_{avg, iR\text{-}corr}$ values. In Fig. 9a, $V_{avg, iR\text{-}corr}$ for the x = 0 electrode drops by 162 mV during charge and 87 mV during discharge within the initial 25 cycles. The voltage fade then declines in the following cycles. In Fig. 9b, the $V_{avg, iR\text{-}corr}$ for the x = 0.1 electrode decreases by 128 mV during charge and 109 mV during discharge within the 25 cycles, and the fade rate is retarded in the following cycles.

Figure 10 summarizes the effect of Cr substitution on the voltage fade in $Li_{1.2}Ni_{0.2-x/2}Mn_{0.6-x/2}Cr_xO_2$ (x = 0, 0.05, 0.1, and 0.2). The relative voltage fade, which is defined as decay in $V_{avg. iR\text{-}corr}$ relative to $V_{avg. iR\text{-}corr}$ at the 2nd cycle, is used for the comparison. In Fig. 10a, the Cr-substituted electrodes show lower voltage fade rates during charge compared to that for the x = 0 electrode (after 50 cycles, ~3.5% and 5% decay, respectively, for the Cr-substituted and x = 0 electrodes). However, as shown in Fig. 10b, the Cr substitution does not retard the voltage fade during discharge (~3.5% decay after 50 cycles). The initial fade rate actually appears to be higher in the Cr-substituted electrodes. While the charge voltage is related to the energy that a battery cell consumes during charge, the discharge voltage is linked to the energy that is released from the cell during discharge. Therefore, it is not advantageous from a practical point of view that the Cr substitution delays only the charge voltage fade, but not the discharge voltage fade.

The voltage fade in lithium-manganese-rich layered-layered composite oxides is induced by the transition metal migration and subsequent structural transition from the layered structure. This structural relaxation is accelerated by lithium and oxygen loss from the transition metal layers during the activation of the Li_2MnO_3 component. Prior works has suggested that the oxygen loss is critical for the irreversible migration of transition metals, such as manganese and nickel ions, from their original octahedral sites in transition metal layers to lithium layers, and this oxygen vacancy-assisted migration of transition metals promotes the formation of spinel-like phases.[13, 15] Therefore, it can be inferred from the reduced Li_2MnO_3 activation that the Cr-substituted electrodes have less structural destabilization, which is caused by the lithium and oxygen loss from the transition metal layers in the Li_2MnO_3 domain. However, the insignificant effect of the Cr substitution on mitigating the voltage fade observed in this study suggests that Cr substitution has a negative effect that cancels out the positive effect of preserving the Li_2MnO_3 domains. One hypothesis is the structural destabilization induced by only quasi-reversible Cr^{6+} movement. Besides the lithium and oxygen loss from the transition metal layers, the significant disposition of Cr^{6+} ions from their original octahedral sites in the transition metal layers may further accelerate the irreversible migration of other transition metal ions, such as Mn and Ni, to the lithium layer and, in turn, cause structural relaxation to a lower voltage phase, such as spinel-like phase fractions.

4. Conclusions

In order to explore stopping voltage fade in LMR-NMC cathode materials, we have examined the effect of Cr substitution on the electrochemical response, specifically

in lithium-manganese-rich $0.5Li_2MnO_3 \bullet 0.5LiNi_{1/2}Mn_{1/2}O_2$ composite cathodes for lithium-ion batteries. With additional charge compensation from the Cr^{3+}/Cr^{6+} redox couple, a large degree of substitution can be demonstrated without a serious sacrifice in initial charge capacity. Furthermore, the initial activation process is suppressed to a minimum, and a larger fractional amount of the Li_2MnO_3 component can be preserved without structural modification due to lithium and oxygen loss from the transition metal layers. However, the initial coulombic efficiency decreases with Cr substitution, and the quasi-equilibrium average voltage comparison revealed that Cr substitution only mitigates the fade in the charge but not discharge voltage. We attribute this insignificant effect of Cr substitution on voltage fade, in spite of a lesser degree of Li_2MnO_3 activation, to an inherent additional instability caused by the Cr^{6+} quasi-reversible migration to the tetrahedral site. Tetrahedral site occupancy accelerates the migration of other transition metal ions and subsequent irreversible structural relaxation to lower voltage phases.

Our results provide the following lessons that can help future development of "layered-layered" composite cathodes: (1) it is possible to achieve high specific capacity without a significant degree of Li_2MnO_3 activation by providing an alternative charge compensation mechanism through redox active cation substitution – the Cr^{3+}/Cr^{6+} redox couple satisfies this criteria, (2) the chemical reversibility of the redox reaction is critical to obtain high reversible capacity – the low initial reversibility of the Cr^{3+}/Cr^{6+} redox couple decreases the reversible capacity of the Cr-substituted electrodes, and (3) the structural stability of the substituted cation itself is equally important to minimize the structural relaxation and related voltage fade during cycling – the migration of Cr^{6+} ions adds structural instability despite lower Li_2MnO_3 activation. Although the voltage fade

was not suppressed, our results validate the concept of redox active cation substitution and provide the framework for future cation substitution strategies by highlighting the electrochemical reversibility and structural stability of the substituent cation itself.

Acknowledgements

Support from the Vehicle Technologies Program, Hybrid and Electric Systems, in particular, David Howell, Tien Duong, and Peter Faguy, at the U.S. Department of Energy, Office of Energy Efficiency and Renewable Energy is gratefully acknowledged. Sector 20 facilities at the Advanced Photon Source, and research at these facilities, are supported by the US Department of Energy - Basic Energy Sciences, the Canadian Light Source and its funding partners, the University of Washington, and the Advanced Photon Source. Use of the Advanced Photon Source, an Office of Science User Facility operated for the U.S. Department of Energy (DOE) Office of Science by Argonne National Laboratory, was supported by the U.S. DOE under Contract No. DE-AC02-06CH11357. The submitted manuscript has been created by UChicago Argonne, LLC, Operator of Argonne National Laboratory ("Argonne"). Argonne, a U.S. Department of Energy Office of Science laboratory, is operated under Contract No. DE-AC02-06CH11357.

References

1. M. M. Thackeray, C. Wolverton and E. D. Isaacs, *Energy Environ. Sci.*, 2012, **5**, 7854.
2. A. Manthiram, *J. Phys. Chem. Lett.*, 2011, **2**, 176.
3. J. B. Goodenough and K.-S. Park, *J. Am. Chem. Soc.*, 2013, **135**, 1167.
4. J. R. Croy, A. Abouimrane and Z. Zhang, *MRS Bull.*, 2014, **39**, 407.
5. M. M. Thackeray, S. H. Kang, C. S. Johnson, J. T. Vaughey, R. Benedek and S. A. Hackney, *J. Mater. Chem.*, 2007, **17**, 3112.
6. M. Jiang, B. Key, Y. S. Meng and C. P. Grey, *Chem. Mater.*, 2009, **21**, 2733.
7. J. Bareño, C. H. Lei, J. G. Wen, S. H. Kang, I. Petrov and D. P. Abraham, *Adv. Mater.*, 2010, **22**, 1122.
8. Y. Li, M. Bettge, B. Polzin, Y. Zhu, M. Balasubramanian and D. P. Abraham, *J. Electrochem. Soc.*, 2013, **160**, A3006.
9. M. Bettge, Y. Li, K. Gallagher, Y. Zhu, Q. Wu, W. Lu, I. Bloom and D. P. Abraham, *J. Electrochem. Soc.*, 2013, **160**, A2046.
10. A. R. Armstrong, M. Holzapfel, P. Novak, C. S. Johnson, S. H. Kang, M. M. Thackeray and P. G. Bruce, *J. Am. Chem. Soc.*, 2006, **128**, 8694.
11. F. L. Mantia, F. Rosciano, N. Tran and P. Novák, *J. Electrochem. Soc.*, 2009, **156**, A823.
12. Y. Okamoto, *J. Electrochem. Soc.*, 2012, **159**, A152.
13. D. Qian, B. Xu, M. Chi and Y. S. Meng, *Phys. Chem. Chem. Phys.*, 2014, **16**, 14665.
14. H. Kddir and R. Benedek, *Chem. Mater.*, 2014, **26**, 2407.
15. M. Gu, I. Belharouak, J. Zheng, H. Wu, J. Xiao, A. Genc, K. Amine, S. Thevuthasan, D. R. Baer, J.-G. Zhang, N. D. Browning, J. Liu and C. Wang, *ACS Nano*, 2012, **7**, 760.
16. M. Bettge, Y. Li, B. Sankaran, N. D. Rago, T. Spila, R. T. Haasch, I. Petrov and D. P. Abraham, *J. Power Sources*, 2013, **233**, 346.
17. I. Bloom, L. Trahey, A. Abouimrane, I. Belharouak, X. Zhang, Q. Wu, W. Lu, D. P. Abraham, M. Bettge, J. W. Elam, X. Meng, A. K. Burrell, C. Ban, R. Tenet, J. Nanda and N. Dudney, *J. Power Sources*, 2014, **249**, 509.
18. Eungje Lee, Brandon R. Long, Jason R. Croy, Mahalingam Balasubramanian, Baris Key, Victor A. Maroni, Michael M. Thackeray, and Christopher S. Johnson, presented in part at the 225th ECS Meeting, Orlando, May, 2014.
19. E. Lee, R. Koritala, D. J. Miller, and C. S. Johnson, *J. Electrochem. Soc.*, 2015, **162**, A322.
20. Z. H. Lu and J. R. Dahn, *J. Electrochem. Soc.*, 2002, **149**, A1454.
21. N. K. Karan, D. P. Abraham, M. Balasubramanian, M. M. Furczon, R. Thomas and R. S. Katiyar, *J. Electrochem. Soc.*, 2009, **156**, A553.
22. B. Ammundsen, J. Paulsen, I. Davidson, R.-S. Liu, C.-H. Shen, J.-M. Chen, L.-Y. Jang and J.-F. Lee, *J. Electrochem. Soc.*, 2002, **149**, A431.
23. D. Kim, J. Gim, J. Lim, S. Park and J. Kim, *Mater. Res. Bull.*, 2010, **45**, 252.
24. S.-J. L. Kang, *Sintering: densification, grain growth and microstructure*, Elsevier Butterworth Heinemann, Burlington, 2005.

25. G. Singh, R. Thomas, A. Kumar and R. S. Katiyar, *J. Electrochem. Soc.*, 2012, **159**, A410.
26. I. Belharouak, G. M. Koenig Jr., J. Ma, D. P. Wang and K. Amine, *Electrochem. Commun.*, 2011, **13**, 232.
27. S. H. Park, S. H. Kang, C. S. Johnson, K. Amine and M. M. Thackeray, *Electrochem. Commun.*, 2007, **9**, 262.
28. D. Kim, G. Sandi, J. R. Croy, K. G. Gallangher, S. H. Kang, E. Lee, M. D. Slater, C. S. Johnson and M. M. Thackeray, *J. Electrochem. Soc.*, 2013, **160**, A31.
29. B. R. Long, J. R. Croy, J. S. Park, J. G. Wen, D. J. Miller and M. M. Thackeray, *J. Electrochem. Soc.*, 2014, **161**, A2160.
30. M. Balasubramanian, J. McBreen, I. J. Davidson, P. S. Whitfield and I. Kargina *J. Electrochem. Soc.*, 2002, **149**, A176.
31. C. M. Julien and M. Massot, *Mater. Sci. Eng. B*, 2003, **100**, 69.
32. D. Y. W. Yu, K. Yanagida, *J. Electrochem. Soc.*, 2011, **158**, A1015.
33. Z. H. Lu and J. R. Dahn, *J. Electrochem. Soc.*, 2003, **150**, A1044.
34. K. G. Gallagher, J. R. Croy, M. Balasubramanian, M. Bettge, D. P. Abraham, A. K. Burrell and M. M. Thackeray, *Electrochem. Commun.*, 2013, **33**, 96.

Figure Captions

Figure 1. Particle morphologies of as-synthesized $Li_{1.2}Ni_{0.2-x/2}Mn_{0.6-x/2}Cr_xO_2$ powder samples (x = 0 – 0.2).

Figure 2. (a) XRD patterns and (b) UV Raman spectra of as-synthesized $Li_{1.2}Ni_{0.2-x/2}Mn_{0.6-x/2}Cr_xO_2$ powder samples. Asterisks in (a) indicate peak positions corresponding to Li-Mn_6 superstructure orderings.

Figure 3. Initial voltage profiles of $Li_{1.2}Ni_{0.2-x/2}Mn_{0.6-x/2}Cr_xO_2$ (voltage range = 2 – 4.7 V; current rate = 10 mA/g). Arrows indicate the start of activation plateaus.

Figure 4. Initial voltage profiles and coulombic efficiency (inset) of $Li_{1.2}Ni_{0.2-x/2}Mn_{0.6-x/2}Cr_xO_2$ (voltage range = 2 – 4.2 V; current rate = 10 mA/g).

Figure 5. Normalized Cr K-edge XANES of the $Li_{1.2}Ni_{0.1}Mn_{0.5}Cr_{0.2}O_2$ electrodes at various states of charge.

Figure 6. Cycle performance of the $Li_{1.2}Ni_{0.2-x/2}Mn_{0.6-x/2}Cr_xO_2$ electrodes.

Figure 7. Voltage profiles of the $Li_{1.2}Ni_{0.2-x/2}Mn_{0.6-x/2}Cr_xO_2$ electrodes at selected cycle numbers.

Figure 8. Normalized differential capacity (1/Q*(dQ/dV)) plots of the $Li_{1.2}Ni_{0.2-x/2}Mn_{0.6-x/2}Cr_xO_2$ electrodes at selected cycle numbers. The arrows indicate the major peak shifts on cycling.

Figure 9. Changes in average voltages as a function of cycle number for (a) x = 0 and (b) x = 0.1 in $Li_{1.2}Ni_{0.2-x/2}Mn_{0.6-x/2}Cr_xO_2$ (open symbol = apparent average voltage, V_{avg}; solid symbol = resistance corrected average voltage, $V_{avg, iR-corr}$).

Figure 10. Plots of relative voltage fade (VF) in $Li_{1.2}Ni_{0.2-x/2}Mn_{0.6-x/2}Cr_xO_2$ during (a) charge and (b) discharge. The relative voltage fade is defined as the decay in $V_{avg, iR-corr}$ relative to $V_{avg, iR-corr}$ at 2nd cycle.

Table 1. Chemical composition of as-prepared $Li_{1.2}Ni_{0.2-x/2}Mn_{0.6-x/2}Cr_xO_2$ powder samples determined by ICP-MS.

Sample name	x	Target composition	ICP composition
Cr-0	0	$Li_{1.2}Ni_{0.2}Mn_{0.6}O_2$	$Li_{1.20}Ni_{0.20}Mn_{0.60}O_2$
Cr-0.05	0.05	$Li_{1.2}Ni_{0.175}Mn_{0.575}Cr_{0.05}O_2$	$Li_{1.21}Ni_{0.175}Mn_{0.565}Cr_{0.05}O_2$
Cr-0.1	0.1	$Li_{1.2}Ni_{0.15}Mn_{0.55}Cr_{0.1}O_2$	$Li_{1.19}Ni_{0.15}Mn_{0.56}Cr_{0.10}O_2$
Cr-0.2	0.2	$Li_{1.2}Ni_{0.1}Mn_{0.5}Cr_{0.2}O_2$	$Li_{1.20}Ni_{0.10}Mn_{0.51}Cr_{0.19}O_2$

Table 2. Lattice parameters of $Li_{1.2}Ni_{0.2-x/2}Mn_{0.6-x/2}Cr_xO_2$ calculated from whole powder pattern decomposition.

x	a (Å)	c (Å)	Vol. (Å^3)
0	2.8558	14.2319	100.518
0.05	2.8602	14.2308	100.823
0.1	2.8644	14.2558	101.296
0.2	2.8655	14.2666	101.450

Table 3. Initial charge/discharge capacity and coulombic efficiency of $Li_{1.2}Ni_{0.2-x/2}Mn_{0.6-x/2}Cr_xO_2$ cycled at 2 – 4.7 V and a current density of 10 mAh/g.

x	Initial charge capacity (mAh/g)			Initial discharge capacity (mAh/g)	Initial irreversible capacity (mAh/g)	Initial coulombic efficiency (%)
	Total	Slope	Plateau			
0	304.7	98.3	206.4	256.6	48.1	84.2
0.05	286.4	129.8	156.6	225.0	61.4	78.6
0.1	286.4	144.6	141.8	215.9	70.5	75.4
0.2	297.4	191.6	105.8	204.1	93.3	68.6

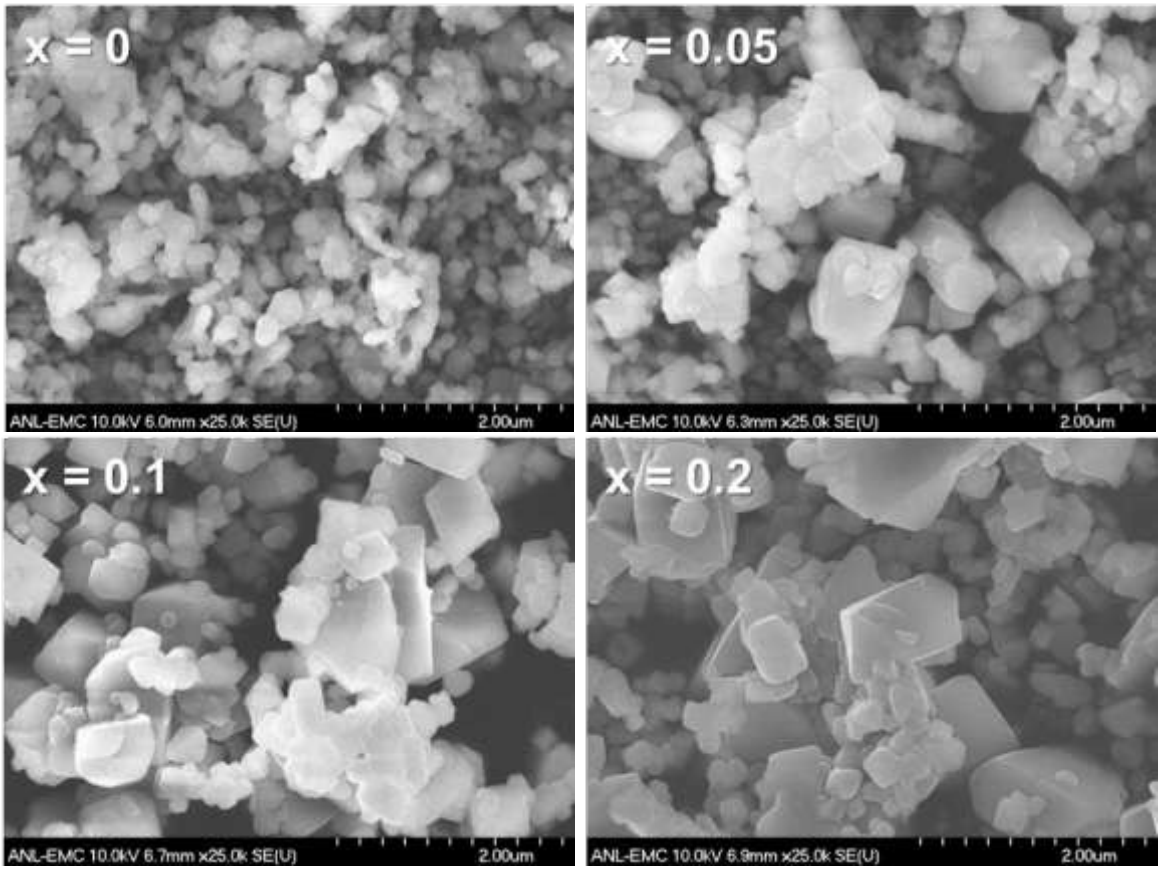

Figure 1. Particle morphologies of as-synthesized $Li_{1.2}Ni_{0.2-x/2}Mn_{0.6-x/2}Cr_xO_2$ powder samples (x = 0 – 0.2).

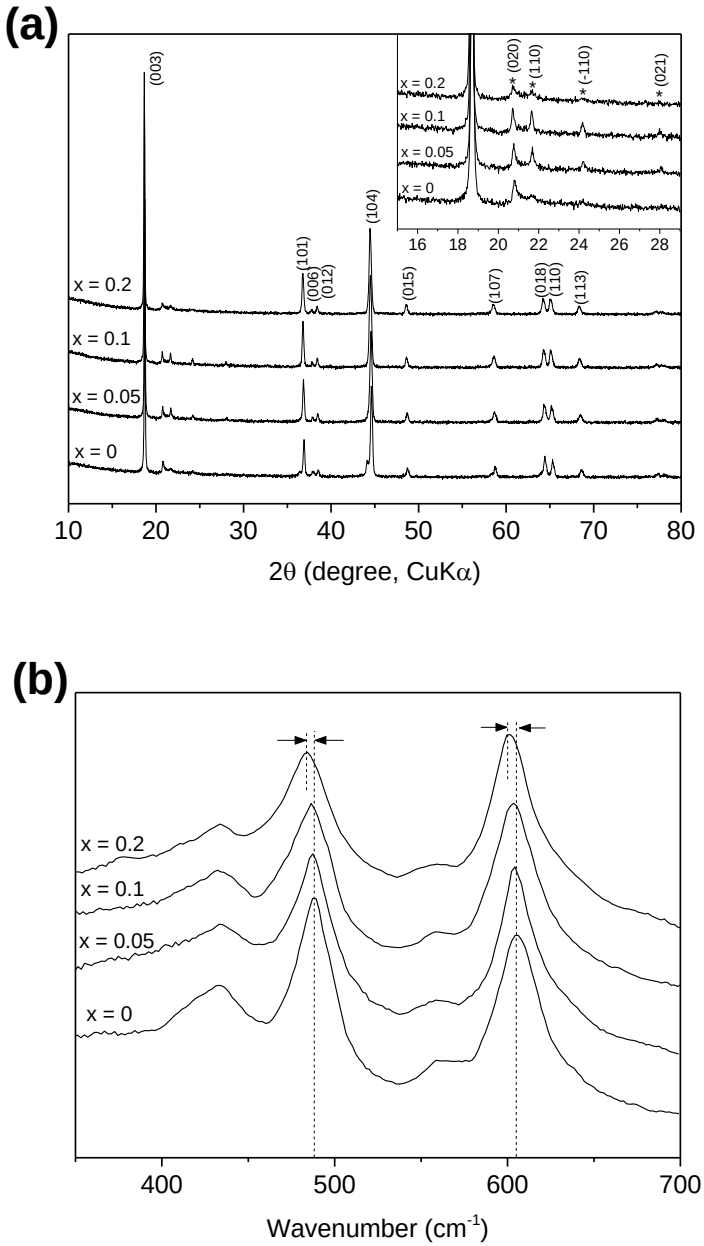

Figure 2. (a) XRD patterns and (b) UV Raman spectra of as-synthesized $Li_{1.2}Ni_{0.2-x/2}Mn_{0.6-x/2}Cr_xO_2$ powder samples. Asterisks in (a) indicate peak positions corresponding to Li-Mn_6 superstructure orderings.

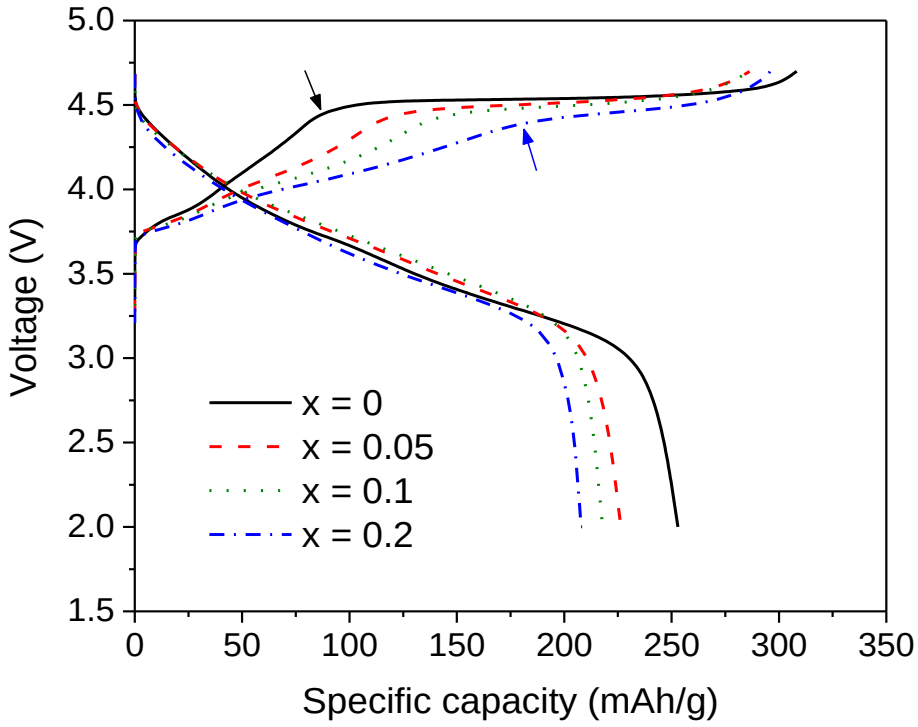

Figure 3. Initial voltage profiles of $Li_{1.2}Ni_{0.2-x/2}Mn_{0.6-x/2}Cr_xO_2$ (voltage range = 2 – 4.7 V; current rate = 10 mA/g). Arrows indicate the start of activation plateaus.

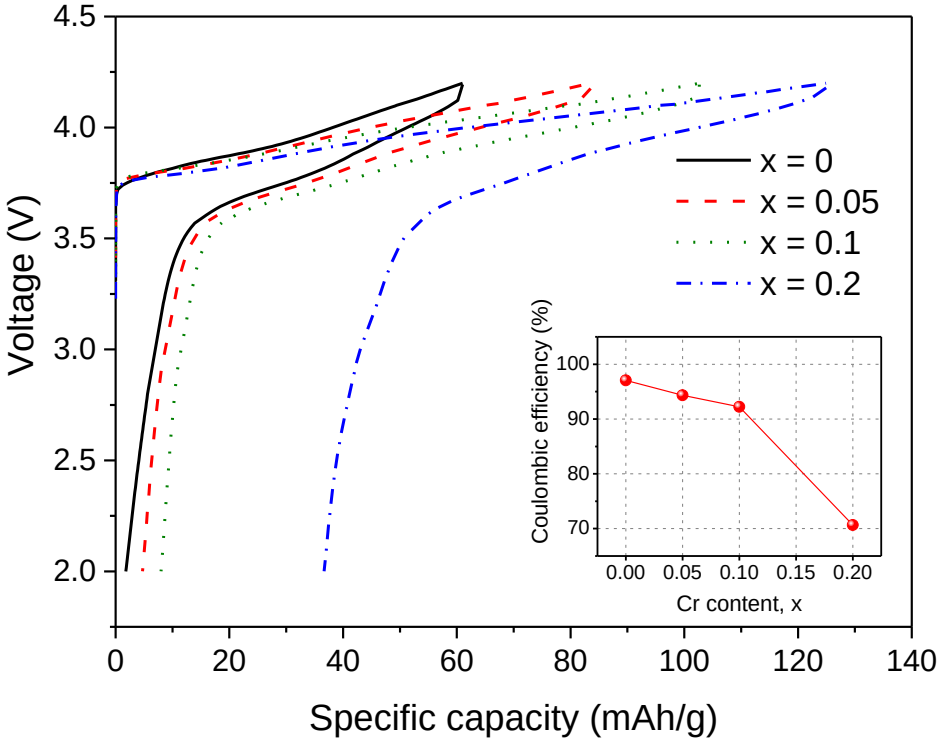

Figure 4. Initial voltage profiles and coulombic efficiency (inset) of $Li_{1.2}Ni_{0.2-x/2}Mn_{0.6-x/2}Cr_xO_2$ (voltage range = 2 – 4.2 V; current rate = 10 mA/g).

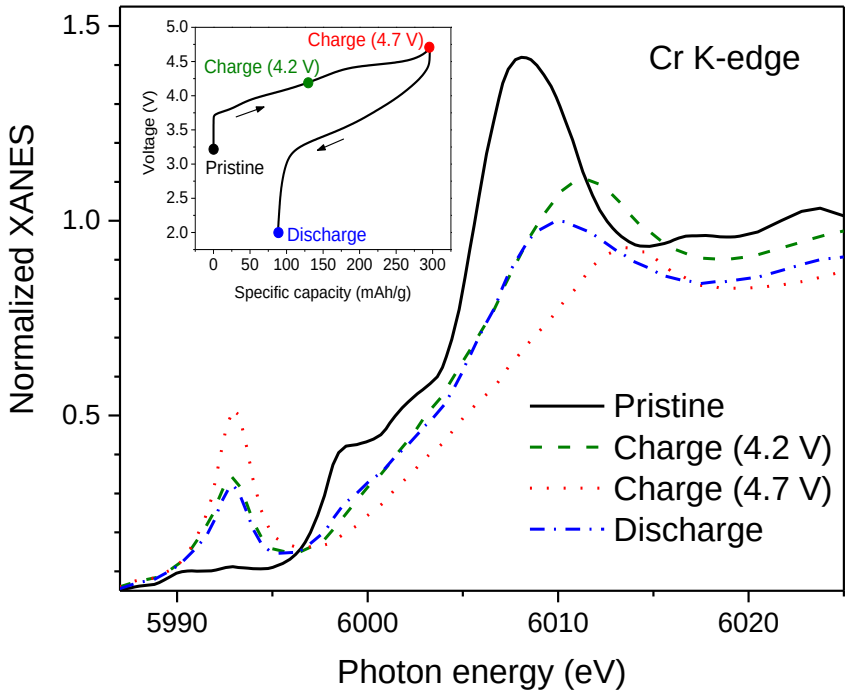

Figure 5. Normalized Cr K-edge XANES of the $Li_{1.2}Ni_{0.1}Mn_{0.5}Cr_{0.2}O_2$ electrodes at various states of charge.

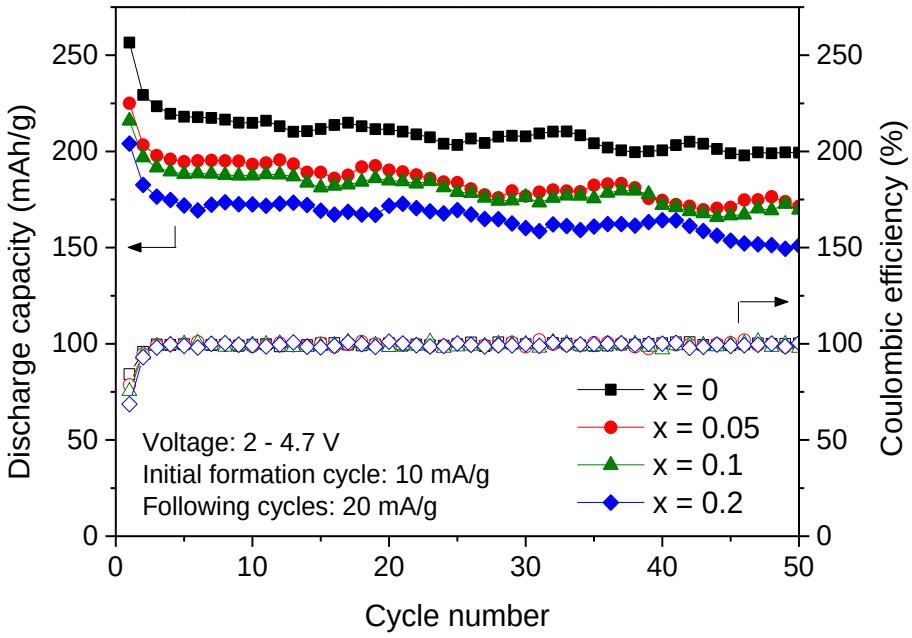

Figure 6. Cycle performance of the $Li_{1.2}Ni_{0.2-x/2}Mn_{0.6-x/2}Cr_xO_2$ electrodes.

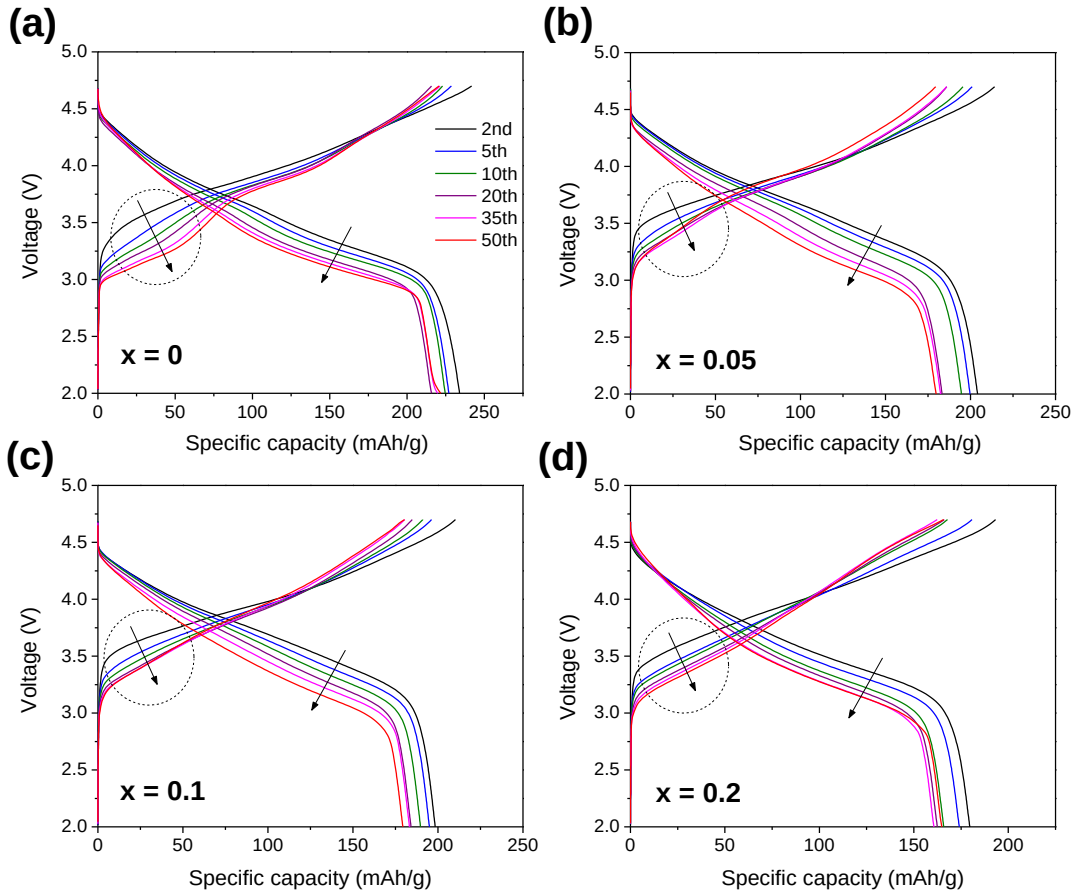

Figure 7. Voltage profiles of the $Li_{1.2}Ni_{0.2-x/2}Mn_{0.6-x/2}Cr_xO_2$ electrodes at selected cycle numbers.

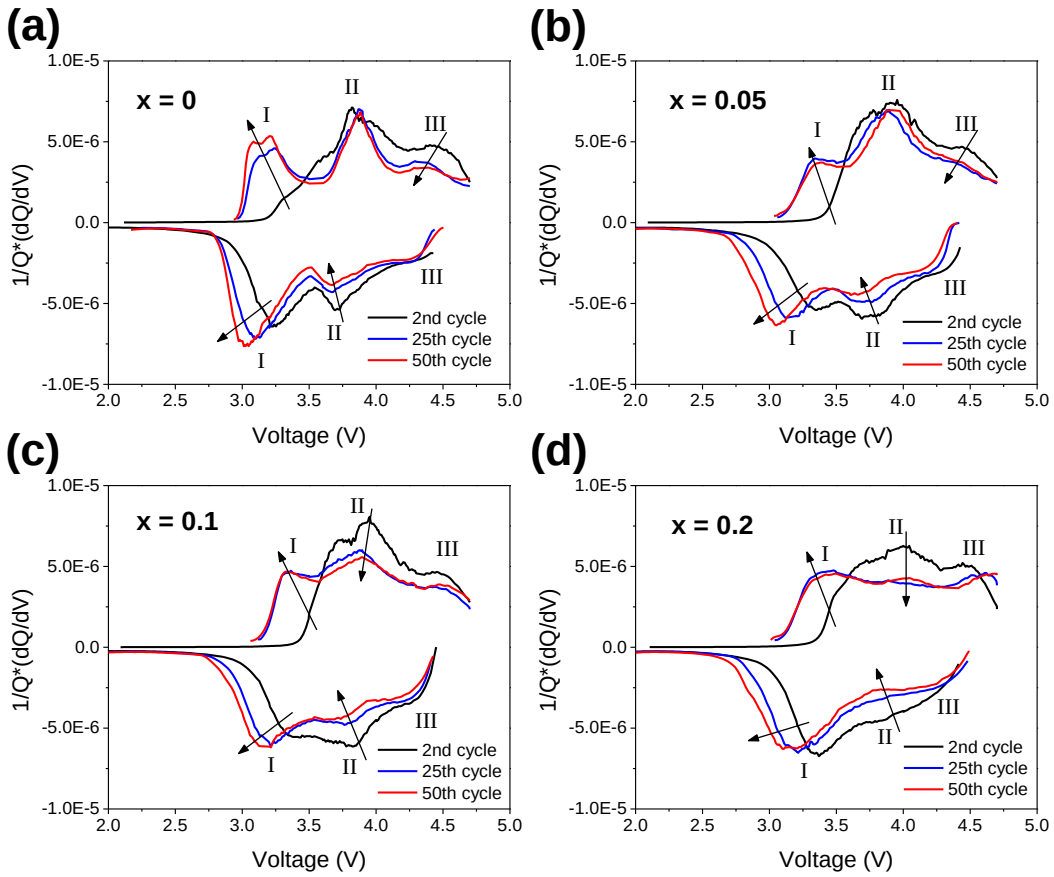

Figure 8. Normalized differential capacity (1/Q*(dQ/dV)) plots of the $Li_{1.2}Ni_{0.2-x/2}Mn_{0.6-x/2}Cr_xO_2$ electrodes at selected cycle numbers. The arrows indicate the major peak shifts on cycling.

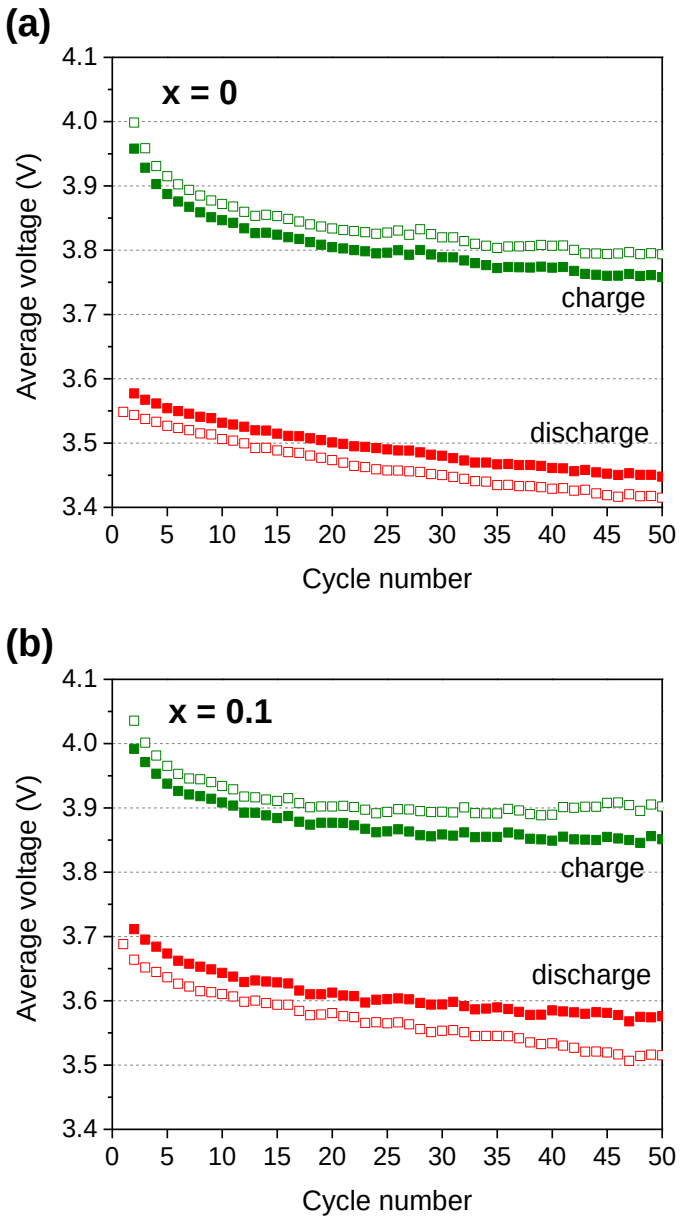

Figure 9. Changes in average voltages as a function of cycle number for (a) x = 0 and (b) x = 0.1 in $Li_{1.2}Ni_{0.2-x/2}Mn_{0.6-x/2}Cr_xO_2$ (open symbol = apparent average voltage, V_{avg}; solid symbol = resistance corrected average voltage, $V_{avg,\ iR\text{-}corr}$).

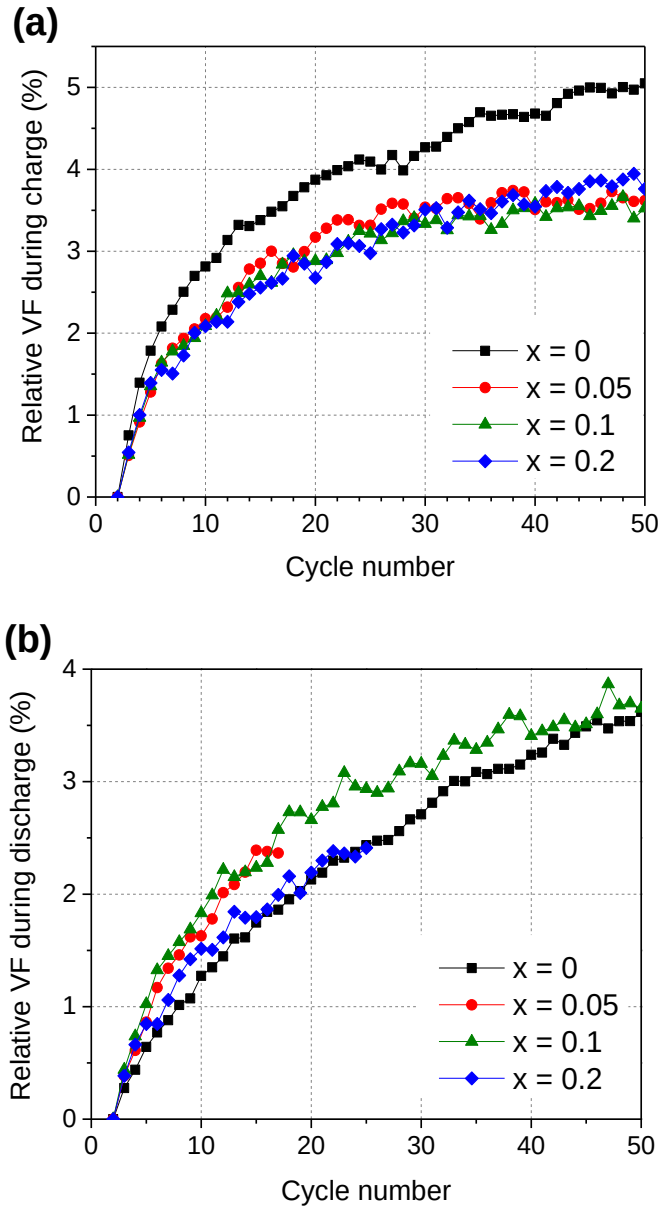

Figure 10. Plots of relative voltage fade (VF) in $Li_{1.2}Ni_{0.2-x/2}Mn_{0.6-x/2}Cr_xO_2$ during (a) charge and (b) discharge. The relative voltage fade is defined as the decay in $V_{avg,\ iR\text{-}corr}$ relative to $V_{avg,\ iR\text{-}corr}$ at 2^{nd} cycle.

Role of Cr^{3+}/Cr^{6+} Redox in Chromium-substituted Li_2MnO_3•$LiNi_{1/2}Mn_{1/2}O_2$ Layered Composite Cathodes: Electrochemistry and Voltage Fade

Eungje Lee and Christopher S. Johnson, et al.

Graphical abstract

The substitution of chromium into the composite Li_2MnO_3•$LiNi_{1/2}Mn_{1/2}O_2$ cathode dramatically affects the voltage plateau response during the initial electrochemical activation process. The resultant Cr^{3+}/Cr^{6+} redox couple is electrochemically and spectroscopically observed coincident with the destabilizing high voltage reaction of the Li_2MnO_3 component. Unfortunately the Cr substitution, despite its confirmed movement from octahedral (Cr^{3+}) to tetrahedral (Cr^{6+}) coordination does not alleviate the voltage fade process in this class of materials.